

# **Chapter 7 *Numerical Results***

## **7.1. General**

The tectonic setting of the test area together with the results of other studies on the deformation of the Kenai Peninsula was briefly reviewed in Chapter 2. In this chapter, the crustal deformation of this area is analyzed in two and three dimensions. The 3D-Lagrangian and Isoparametric approaches of Chapters 3 and 4 will be applied to the GPS results of the crustal deformation GPS array in the Kenai Peninsula.

To discuss on obtained results, applied GPS data is firstly reviewed. GPS data is processed using the Bernese GPS software 4.2 (Beutler et al., 2001). Therefore, adopted processing strategy is introduced before discussing on the GPS results. The GPS results are used in both two- and three-dimensional analysis of deformations. After giving the two-dimensional results of deformation analysis, three-dimensional results of the Lagrangian and Isoparametric representations of deformation are given. To analyze the effect of vertical deformations on horizontal ones, the horizontal components of the 3D-results are compared to the traditional two-dimensional ones. It is also shown how the independent results of the other studies, which were reviewed in Chapter 2, support the three-dimensional results of this work in both horizontal and vertical dimensions. Finally, the statistical inference of Chapter 5 is used for analyzing the significance of the spatial variation of deformations in this area.

## **7.2. GPS Data, Analysis and Results**

### **7.2.1. GPS Data**

GPS measurements were initiated in Kenai in 1993. Since then, several campaign surveys have been carried out in this and the surrounding area. The initial goal of these surveys was to characterize the cumulative 30-years averaged post-seismic response of the Earth's crust by comparing the elevations of modern GPS surveys to the elevations that were determined shortly after the earthquake by spirit leveling (Freymueller et al., 2000). Therefore in

initial campaigns, GPS measurements were carried out at existing benchmarks that were established in the 1964 leveling survey.

The GPS data of seven campaigns: 1995, 1996, 1997, 1998 (.06 and .09), 1999 and 2000 were downloaded through the University NAVSTAR COnsortium (UNAVCO) Boulder facility for this study. The data have been provided by the University of Alaska and is also accessible to download from the Alaska Deformation Array (AKDA) data center in this university.

To apply the three-dimensional approaches of this research, GPS stations that have been remeasured in at least two successive campaigns are required. Therefore, from the available campaigns a set of 16 stations of the two successive campaigns 1996 and 1998.06 have been selected. Ten benchmarks of the leveling survey of 1964; that is the stations: T19D, CROS, K76D, GRAV, DAHL, M78D, S79R, H81D, Z82A and HOMA (Cohen et al., 1995; Cohen and Freymueller, 1997) are included in the selected set of GPS stations. The locations of these stations and the topography of this area are shown in Figure 7.1. GPS stations are shown by small triangles. GPS stations that are collocated with leveling benchmarks of the

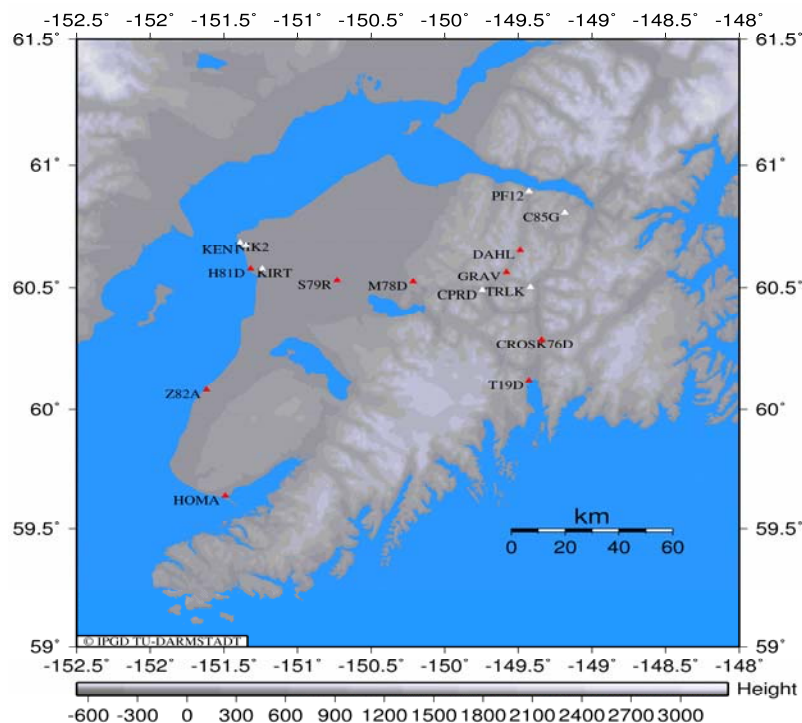


Figure 7.1: The configuration of the GPS stations in this study.

survey 1964 are shown in red. The station names are the four character abbreviations that were conventionally used for processing the GPS data. The maximum distance of station is 181130.87 km between station HOMA and PF12. The minimum distance of stations is 22.61 m between stations K76D and CROS. The minimum height difference between stations is 0.0927 between stations CROS and K76D and the maximum height difference between stations is 363.7373 m between stations DAHL and NIK2.

Three regional permanent stations were also added to this configuration mainly to address the reference frame issue for analyzing the GPS measurements (Becker et al., 2002). These include stations KEN1, in the city of KENAI, KOD1, in the Kodiak Islands, from the CORS permanent GPS network and the IGS station FAIR in Fairbanks. The locations of the two reference stations FAIR and KOD1 are shown in the Figure 2.2.

### **7.2.1.1. Campaign 1996**

Observations of this campaign were carried out in 10 successive days (sessions) starting from the 1<sup>st</sup> of June 1996, DOY 153-GPS Week 855, and lasted on the 10<sup>th</sup> of June, DOY 162-GPS Week 857. Dual frequency GPS receivers: Trimble 4000SSI and Trimble 4000SSE were used together with antenna types TRM22020.00 and TRM14532.00 in these measurements. Carrier beat phases were measured in full wavelength. At all stations except Z82A, on DOYs 156 and 157, M78D, on DOY 158, and H81D, on DOY 159, antennas were equipped with ground plates to suppress the multi-path effect. Table 7.1 provides an overview for the contribution of individual stations in the daily measurements of this campaign. The list contains station numbers and station names, conventionally used in computations. It also shows the observation scenario (the stations that have been incorporated in the observation) of each session. Typically, all sessions are 23h: 59m: 00s long. In all sessions there is at least one station whose average observation time span is less than 24 hours, mostly about 8 hours and less. This situation is especially remarkable at the sites that were occupied once or twice during this campaign. Different antenna types were used in the regional stations. ROGUE SNR-8000 receiver was used with DORNE MARGOLIN R antenna in the IGS station FAIR. ASHTECH Z-XII 3 receivers and ASH700829.3 antennas were used in the permanent sta-

tions KEN1 and KOD1. Sampling interval of the carrier beat phases is 30 seconds at all stations of network within the Kenai Peninsula. Therefore, observations of the regional permanent sites were downloaded and used at the same sampling rate.

TOTAL NUMBER OF STATIONS:		19	0000000001									
NUM	STATION	#FIL	1	2	3	4	5	6	7	8	9	0
1	FAIR	10	X	X	X	X	X	X	X	X	X	X
2	KOD1	10	X	X	X	X	X	X	X	X	X	X
3	KEN1	10	X	X	X	X	X	X	X	X	X	X
4	C85G	2		X	X							
5	CPRD	10	X	X	X	X	X	X	X	X	X	X
6	CROS	2		X	X							
7	DAHL	9	X	X	X	X	X	X	X	X		
8	GRAV	3	X	X	X							
9	H81D	2		X	X							
10	HOMA	10	X	X	X	X	X	X	X	X	X	X
11	K76D	1	X									
12	KIRT	10	X	X	X	X	X	X	X	X	X	X
13	M78D	2		X	X							
14	NIK2	5	X	X	X	X	X					
15	PF12	2		X	X							
16	S79R	2		X	X							
17	T19D	2		X	X							
18	TRLK	10	X	X	X	X	X	X	X	X	X	X
19	Z82A	2		X	X							

**Table 7.1: The repeatability of the GPS sites in observation scenario of campaign 1996.**

### 7.2.1.2. Campaign 1998

The observations of this campaign were also carried out in 10 successive days starting on the 1<sup>st</sup> of June 1998, DOY 152-GPS Week 960, and lasted on the 10<sup>th</sup> of June, DOY 161-GPS Week 961. Dual frequency GPS receivers: Trimble 4000SSI and Trimble 4000SSE together with TRM22020.00 antenna were used to carry out the measurements. Carrier beat phases were measured in full wavelength. At all stations antennas were equipped with ground plates to suppress the multi-path effect. Table 7.2 provides an overview similar to Table 7.1 for the contribution of individual stations in the various days of this campaign. The same parameters as Table 7.1 are used in this table too. All sessions are nominally 23h: 59m: 00s long. There are at least two stations whose average observation time span is remarkably less than 24 hours, mostly about 8 hours. Especially, this situation is considerable at the sites

that are occupied once or twice during this campaign. At all of these stations, GPS measurements were initiated after about 15:00pm in the local time zone. The same hardware (receiver and antenna types) as the campaign 1996 was used in the regional permanent sites during the measurements of this campaign. Sampling interval was again 30 seconds at all stations. Therefore, GPS measurements at permanent sites were also downloaded and used at this sampling rate.

TOTAL NUMBER OF STATIONS:		19	0000000001								
NUM	STATION	#FIL	1	2	3	4	5	6	7	8	9
1	FAIR	9	XXXX	XXXXX							
2	KOD1	7	XXXX	XXX							
3	KEN1	10	XXXXXXXXXXXX								
4	C85G	2	XX								
5	CPRD	9	XXXXX	XXXX							
6	CROS	1		X							
7	DAHL	6	XXXXXX								
8	GRAV	3	XX	X							
9	H81D	2	X	X							
10	HOMA	9	XXXXXXXXXX								
11	K76D	2	X		X						
12	KIRT	2	XX								
13	M78D	2		XX							
14	NIK2	4		XXXX							
15	PF12	2		XX							
16	S79R	2	X	X							
17	T19D	2	XX								
18	TRLK	8	XXXXXXXXXX								
19	Z82A	3	XXX								

**Table 7.2: The repeatability of the GPS sites in observation scenario of campaign 1998.**

### 7.2.2. Analysis

The Bernese GPS software version 4.2 was used for processing the data. The steps to be taken for processing the GPS data in this software are illustrated in the flow diagram of Figure 7.2 (Beutler et al., 2001).

After setting up a campaign, observation files were transferred from the RINEX (Receiver INdependent EXchange) ASCII format (Gurtner et al., 1994) into the Bernese binary format. It was also necessary to concatenate some RINEX files before transforming them to

the Bernese binary format. As the result the code and phase zero difference header and observation files were produced.

The IGS (International GPS Service for Geodynamics) antenna phase center offset and variation calibration table (Rothacher et al., 1995) is used to avoid the systematic effect of using different antenna types in the regional and the local stations.

To get high precision results, CODE (Center of Orbit Determination in Europe) precise orbits and earth rotation parameters were used (Beutler et al., 2001). Minimum elevation cut off angle was set to 10 degrees for processing the data in all epochs (Rothacher et al., 1998).

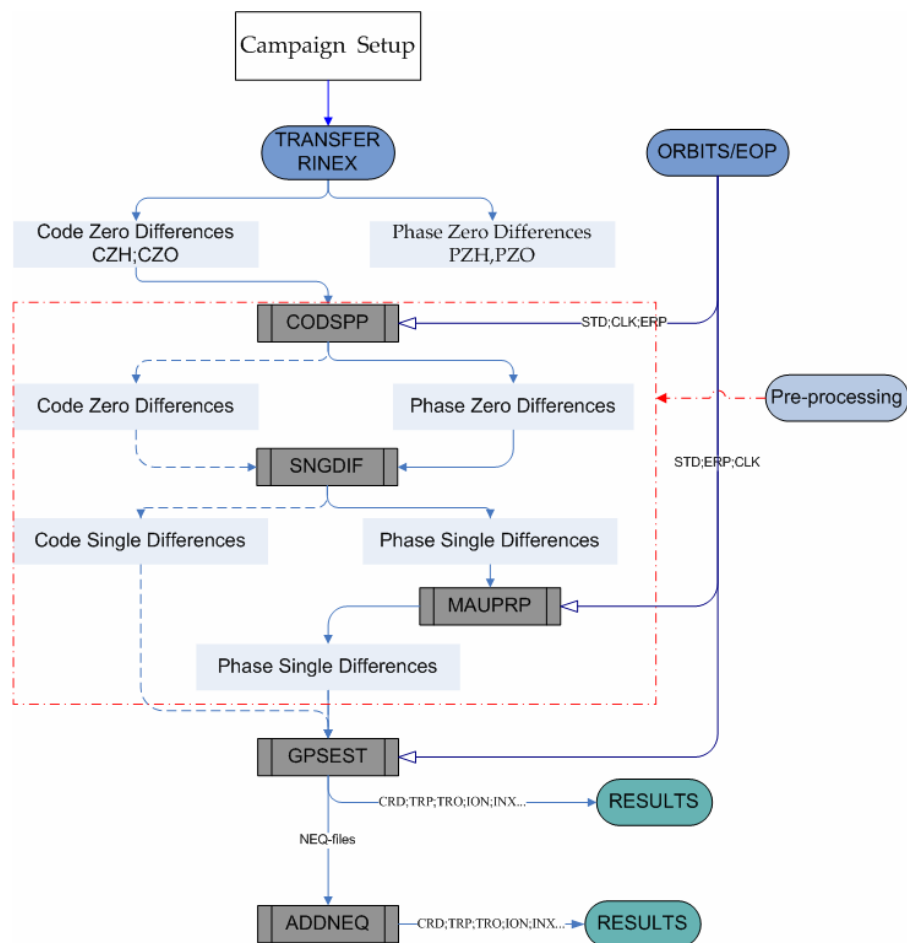


**Figure 7.2: The flow diagram for processing the GPS data using the Bernese GPS data processing software.**

Carrier beat phases were pre-processed for detecting the cycle-slips and their repair. This was done in automatic mode using L3 frequency and L3 triple- difference solutions. Not only in the pre-processing of the data but also in the final steps of parameters estimation and the computation of the combined solution, the input options were mostly considered as the default values that are recommended by the Bernese team.

Short and long baselines were both processed simultaneously in epoch 1996. For epoch 1998, once this was done separately for short and long baselines. Then a procedure similar to the previous epoch was taken to see probable differences in the quality of final results. OBS-MAX strategy was used for establishing the baselines in both campaigns.

Observations whose residuals were larger than 0.003 m were considered as outliers and marked out in the observation files during the data snooping process.

Initial phase ambiguities were resolved using the QIF (Quasi Ionosphere Free) strategy in both campaigns (Mervart, 1995). Site-specific troposphere parameters were estimated at each station and each session to account for the effect of troposphere error when the ambiguities were being resolved. Generally, 12 troposphere parameters were estimated at each station. When the observation time span was less than 24 hours, the number of the site-specific troposphere parameters was reduced. For this purpose, the number of the site-specific troposphere parameters was tuned in such a way that estimated troposphere parameters were stochastically meaningful (they were comparable to their RMS values). For long baselines (baselines longer than 10 km) local Ionosphere models (Wild, 1994; Schaer, 1999) that were estimated with the same data set, were used to improve the process of ambiguity resolution.

The consistency of the resolved integer ambiguities with the mathematical models that have been implemented in the processing software was checked. This was done through the comparison of the a-posteriori variance of unit weight in the float solution (obtained from the first run of the program GPSEST in which the ambiguities are treated as unknown parameters) and that of the fixed solution (obtained in the third run of this program, in which the resolved integer L1 and L2 ambiguities are introduced as known parameters to the system of normal equations). A consistent integer ambiguity results in a smooth change in the a-posterior variance of unit weight whereas an inconsistent one can produce abrupt variations in the estimates of this parameter.

As a measure for the precision of the GPS results, RMS repeatabilities of the stations coordinates are normally studied. RMS repeatability is defined as the scatter of daily solutions from the final campaign solution. RMS repeatabilities are one of the by products in the final step of the GPS data processing by Bernese where the daily solutions are combined to obtain the campaign or combined solution. The RMS repeatabilities of the two campaigns in this study are shown in Figure 7.3 and Figure 7.4.

To improve the repeatability of daily solutions and thereby the overall precision of the final GPS results, the normal equation of the DOY 155 in campaign 1996 and the normal equations of the DOYs 158 and 161 in campaign 1998 were not included for estimating the corresponding combined solutions of each campaign.

Repeatability results clearly show the poorer quality of the GPS results in the height component as compared to the horizontal components of the stations position. Moreover, they clearly show that the obtained formal errors for the campaign solutions are too optimistic to be taken into account. This is mainly due to the fact that systematic and time correlated error sources are neglected in the stochastic model for processing the GPS measurements (Leinen et al., 1999). To get a realistic accuracy for the GPS results, the formal covariance matrices of the campaign solutions are scaled by a factor of 14.73 in campaign 1996 and 16.86 in the campaign 1998.06. Table 7.3 gives the mean formal errors of the stations coordinates together with their scaled values.

Campaign	Coordinate Components	Mean Formal Error (mm)	Scaled Mean Formal Error (mm)
1996	Height	0.7526	11.0863
	Latitude	0.3737	05.5044
	Longitude	0.2895	04.2639
1998	Height	0.6526	11.0034
	Latitude	0.3053	05.1467
	Longitude	0.2737	04.6143

**Table 7.3: Mean formal errors and scaled mean formal errors of the coordinate components of campaigns 1996 and 1998.06**

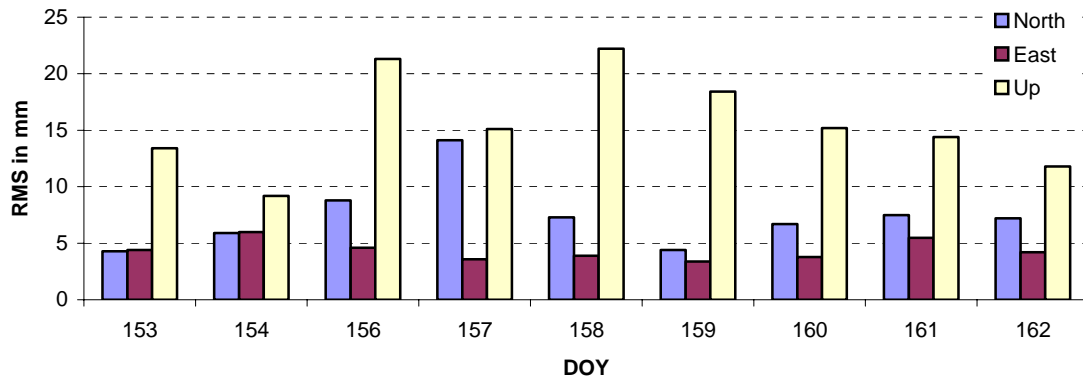


Figure 7.3: The RMS repeatabilities of the Campaign 1996 for the north, east and up components.

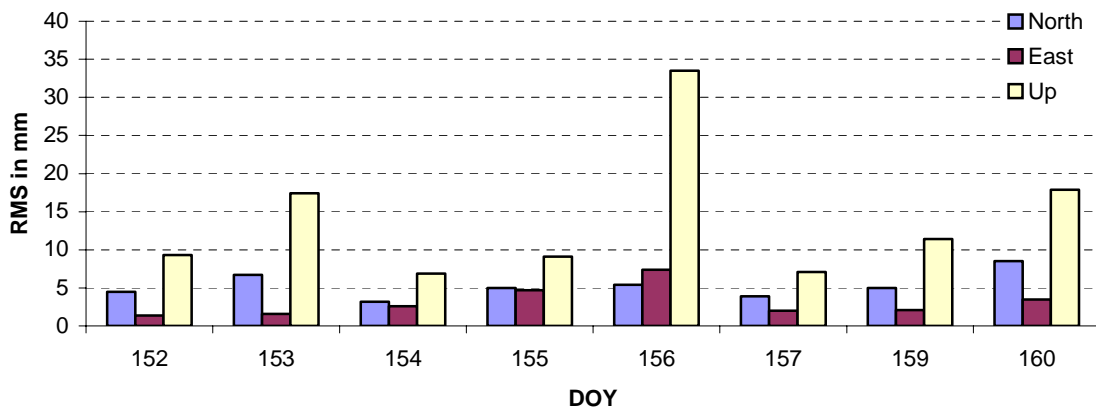


Figure 7.4: The RMS repeatabilities of the Campaign 1998.06 for the north, east and up components.

### 7.2.3. Estimated Velocity Fields

The reference frame is one of the key issues in both the analysis of the GPS measurements and estimating the velocity field. In this respect two points should be carefully taken into account:

- 1) The consistency of the various elements of the reference frame within each epoch,
- 2) The campaign solutions of different epochs should refer to the same realization of the International Terrestrial Reference Frame (ITRF).

The use of the IGS products guarantees the consistency of the different elements of the reference frame like the satellite orbits and Earth orientation parameters. Fulfilling the first requirement above, the combined solution of the campaigns 1996 and 1998.06 were computed in the ITRF realization 1993 and 1996. According to Leinen et al. (1999) and Zweck and Freymueller (2002), to fulfill the second requirement mentioned above, the combined solution of the first epoch was transferred to the reference frame of the second one using a seven parameter Helmert similarity transformation. Horizontal and vertical velocity fields are computed from the coordinate differences. Computed velocity field together with the associated 95% confidence regions obtained from the propagation of scaled errors are shown in Figure 7.5 and Figure 7.6 respectively.

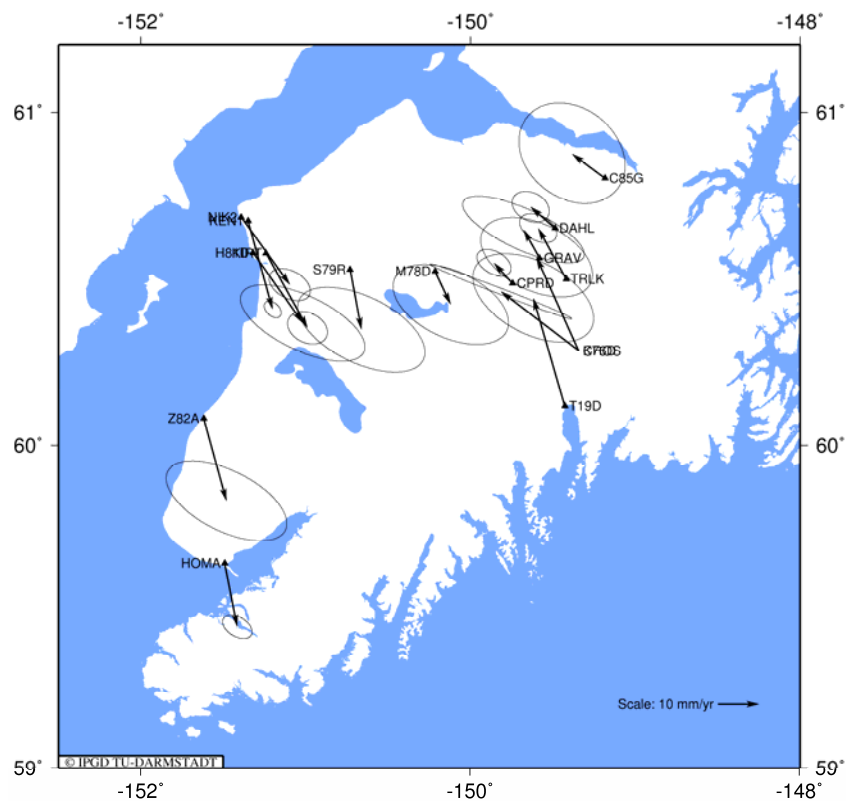


**Figure 7.5 : Estimated horizontal velocity field for the deformation network of the Kenai Peninsula.**

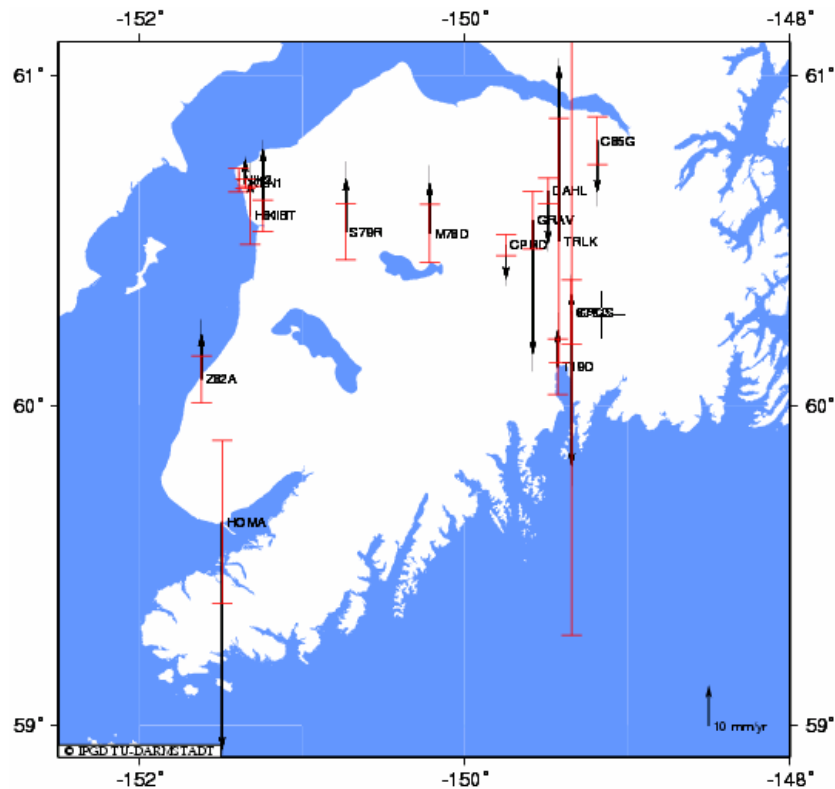


Figure 7.6: Estimated vertical velocity field for the deformation network of the Kenai Peninsula.

Estimated horizontal velocity field suggests a pattern of spatial variation in the deformations of this area according to which the sites in the western Kenai are moving SSE in contrary to the sites of the eastern Kenai whose NNW motions are in accord with the relative motion of the North American and Pacific plates (DeMets et al., 1990). This velocity contrast has been also reported in the previous researches on the deformation of this area (Cohen and Freymueller, 1997; Freymueller et al., 2000; Zweck and Freymueller, 2002). Cohen and Freymueller, (1997) and Freymueller et al. (2000) interpreted the crustal motion of the western Kenai as a delayed or continuing post-seismic transient response of the Aleutian subduction zone to the Alaskan earthquake of 1964. This interpretation was later confirmed by Zweck and Freymueller (2002) using a more comprehensive set of GPS measurements.

### 7.3. Two-dimensional Pattern of Deformation in the Kenai Peninsula

Coordinates and covariance matrices of the Bernese campaign solutions are used as the input information for analyzing the deformation of the study area in two dimensions.

The mathematical formulation of the problem in two-dimensions is based on the Isoparametric representation of infinitesimal deformations (e.g. Love, 1944; Jaeger, 1969 and Flügge, 1972; Chen, 1991):

$$q = e_{xx} l_{AB}^2 + e_{yy} m_{AB}^2 + e_{xy} l_{AB} m_{AB}, \quad q = \frac{\Delta s = s'_{AB} - s_{AB}}{s_{AB}} \quad (7.1)$$

Where baseline lengths  $s_{AB}$  and  $s'_{AB}$  are the length of geodesic  $AB$  on the surface of a reference datum. Rainsford's long-line formulae are used for computing the length of geodesics (Rainsford, 1955). Parameters  $l_{AB}$  and  $m_{AB}$  are the direction cosines of this geodesic on the surface of the reference datum. Direction cosines of geodesic  $AB$  are the inner product of the unit vector that is tangent to the geodesic at (computation) point  $A$  and the base vectors of the curvilinear coordinate axes in which the deformation tensor is to be computed.

Since the method is datum invariant, it is not necessary to transform the campaign solutions to a single reference frame.

Configurations of the computation and contributing points for estimating the parameters of deformation and their variance-covariance matrices are given in Table 7.5. This table also includes the stations that are identified as outliers in the hypothesis test of the a-posteriori variance of unit weight as well as the degree of freedom for each station. Due to the large condition numbers of the normal matrix at stations FAIR and KOD1, the instability of their least-squares solution has been analyzed using the discrete Picard condition. This analysis assures the instability of the corresponding least-squares solutions of the deformation tensor. Therefore, regularization of these solutions is inevitable.

Computed deformation tensors and their variance-covariance matrices are used for estimating principal strains ( $e_I, e_{II}$ ), their orientation and confidence regions. Principal strains and their orientation at each station are given by eigenvalues and eigenvectors of the corresponding deformation tensor at each station. These parameters explain the magnitude and orientation of maximum deformations (e.g. Love, 1944).

Maximum deformations and their orientation are normally used for illustrating the pattern of deformation in the study area. For the Kenai Peninsula, these parameters are shown in Figure 7.7. Compressional principal strains are shown by arrow pairs that are pointing to each other. Pair of arrows that are pointing away exemplify dilatational principal strains. Solid circles are also used for illustrating the surface compression of the Earth's crust at the position of each station. Surface compressions are the sum of the corresponding principal strains or the trace of the deformation tensor, that is  $\Delta = e_I + e_{II} = e_{xx} + e_{yy}$ . The radius of each circle is proportional to the estimated amount of compression. A colored scale bar is also used to simplify the comparison of the compressions of different stations. To increase the clarity in Figure 7.7, estimated confidence regions are not included in this figure. For a detailed comparison of illustrated parameters, corresponding numerical results are also given in Table 7.4.

Station Code	Station Name	Principal Strains ( $\mu$ -strain)				Compression ( $\mu$ -strain)		Azimuth of Maximum Compression, in degrees
		$e_I$	$\sigma_{e_I}$	$e_{II}$	$\sigma_{e_{II}}$	$\Delta$	$\sigma_{\Delta}$	
3	KEN1	0.968	0.073	-1.395	0.090	-0.4266	0.116	132.08
4	C85G	0.294	0.199	-0.634	0.343	-0.3399	0.397	138.24
5	CPRD	0.509	0.123	-0.964	0.155	-0.4554	0.198	137.98
6	CROS	0.498	0.197	-1.032	0.212	-0.5343	0.289	137.56
7	DAHL	0.096	0.098	-0.464	0.161	-0.3677	0.188	149.88
8	GRAV	0.419	0.252	-0.816	0.360	-0.3965	0.439	136.69
9	H81D	0.633	0.339	-1.201	0.416	-0.5679	0.537	136.62
10	HOMA	0.396	0.140	-0.669	0.388	-0.2727	0.413	137.44
11	K76D	0.535	0.243	-1.094	0.278	-0.5582	0.369	137.25
12	KIRT	0.482	0.192	-0.972	0.261	-0.4895	0.324	139.24
13	M78D	0.718	0.351	-1.315	0.451	-0.5970	0.572	137.72
14	NIK2	0.666	0.133	-1.172	0.148	-0.5059	0.199	135.15
16	S79R	0.548	0.380	-1.033	0.460	-0.4859	0.597	138.26
17	T19D	0.646	0.222	-1.131	0.202	-0.4845	0.300	134.78
18	TRLK	0.255	0.096	-0.719	0.126	-0.4633	0.158	142.10
19	Z82A	0.693	0.343	-1.265	0.636	-0.5726	0.722	136.40

**Table 7.4: Results of the two-dimensional analysis of deformations in the Kenai Peninsula (see also Figure 7.7).**

The ongoing post-seismic uplift in Kenai, which was discussed in Chapter 2, justifies the obtained compressional pattern of deformation in this area. It is also seen that the lo-

cation of the maximum compression conforms to the location of maximum uplift in this area (see Figure 2.5).

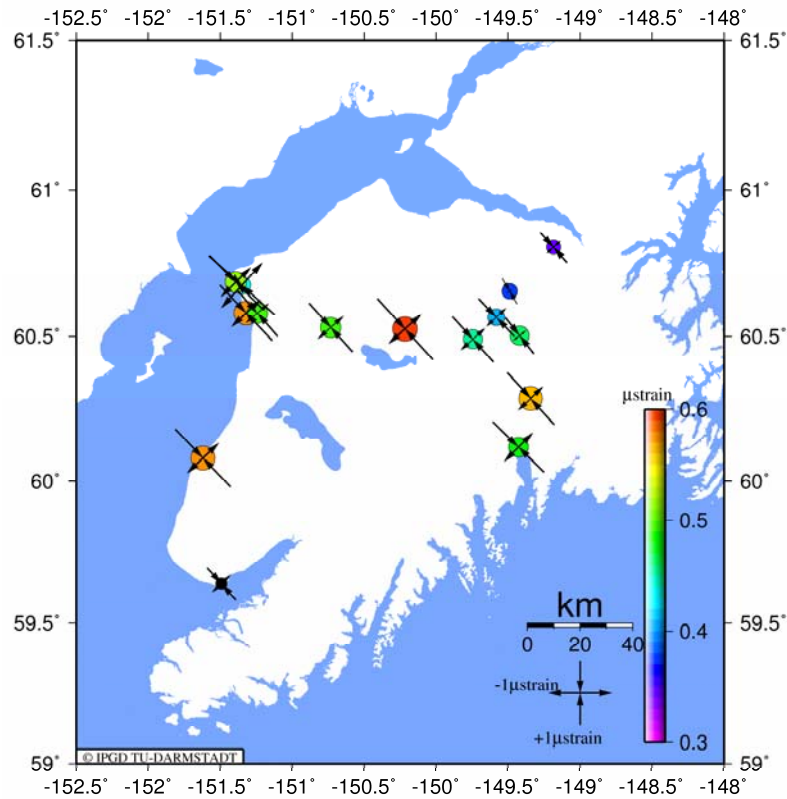


**Figure 7.7: Two-dimensional pattern of deformations in the Kenai Peninsula.**

#### **7.4. Three-Dimensional Pattern of Deformation in the Kenai Peninsula**

Using the algorithms that were described in Chapters 3 and 4 and the GPS results of campaigns 1996 and 1998.06, the three-dimensional pattern of surface crustal deformations is also computed for the Kenai Peninsula. Since Isoparametric representation of deformations is coordinate invariant, Bernese combined epoch solutions can be directly used for the 3D-Isoparametric representation of the post-seismic deformation in this area. For a proper application of Lagrangian approach, campaign solutions should refer to the same reference frame. This was done using a seven parameters Helmert transformation.

Since co-seismic deformations of the 1964 Alaskan event extends from the north to Fairbanks and from the south to the Kodiak Islands (see for example: Hansen and Eckel, 1966; also see Figures 3 and 4 of Chapter 2) both regional and local stations were incorporated in the computation of the 3D-pattern of deformations in this area. Table 7.5 provides an overview for the configuration of computation and contributing points at each station of the GPS network in this area. It can be seen in Figure 7.1 that the two pairs of stations KEN1, NIK2 and CORS, K76D are closely located next to each other. One of the coordinate components in each pair of these stations is much smaller than the other ones ( $\Delta U$  for stations CORS and K76D and  $\Delta N$  for stations KEN1 and NIK2). Consequently, the inclusion of each of them for the computation of deformations at the other one results in the rank deficiency of the system of normal equations (see Chapter 3 for further details). For this reason, station KEN1 has been excluded from the configuration of contributing points for estimating the 3D-deformation tensor at station NIK2 and vice versa. Also, station K76D has not been included in the configuration of contributing points for estimating the deformation tensor at station CORS and vice versa. Moreover, since station PF12 was marked out as an outlier and was removed from the final solution of the Campaign 1998.06, it was not included in computations too.

According to the criteria that were worked out in Chapter 3, the configuration of the GPS network in Kenai is far from an ideal configuration for the analysis of deformation in three dimensions. For example, it is easily seen that some of the stations are nearly located along a longitudinal line. Moreover, the topography of Kenai is also far from an ideal case. The western part of Kenai is relatively flat while there is a rugged topography in its eastern part (see Figure 7.1). Height differences between stations in the western Kenai are small in comparison with the height differences in the eastern Kenai. Therefore, 3D-analysis of deformation in this area is expected to be an ill-conditioned problem. In Chapter 4, the ill conditioning of the problem was assured by inspecting the conditioning of the system of normal equations for both the Isoparametric and Lagrangian representations of deformation. There, the sensitivity of deformation tensors was also analyzed using the diagnosis method of that chapter (see also Appendix B for further details).

The analysis of the discrete Picard condition for both Isoparametric and Lagrangian representations of deformation and for all configurations of computation and contributing points

in the GPS network of this area (see Chapter 4 and Appendix C for more details) proved that the corresponding least-squares solutions are sensitive to perturbations of input parameters. Therefore, to get a stable solution both problems should be regularized. For this purpose, using the method of Chapter 4, for each configuration of computation and contributing points, regularization parameters have been optimally chosen in both Isoparametric and Lagrangian representations of deformations. Then, using the method of truncated singular value decomposition (see Chapter 4) regularized deformation tensors and their variance-covariance matrices are computed in a geocentric Cartesian coordinate system.

Computed deformation tensors and their variance-covariance matrices are then transformed to the spherical coordinate system using the transformation equation of Chapter 3. Principal strains  $e_I$ ,  $e_{II}$ ,  $e_{III}$  and their orientation with respect to the curvilinear coordinate axes are computed again by eigenvalue-eigenvector decomposition of the transformed deformation tensors. Variance-covariance matrices of principal strains are computed using the method of Soler et al., (1991). In addition to that, the surface compression of the Earth ( $\Delta = e_{xx} + e_{yy} + e_{zz} = e_I + e_{II} + e_{III}$ ) is also computed at the position of each station. This invariant parameter is to be used for the assessment of the physical implications of the 3D-results, similar to the way it was done for the two-dimensional results of deformation analysis.

Figure 7.8 illustrates the three-dimensional pattern of deformations. To visualize the horizontal pattern of deformations, the cross section of the deformation quadratic (expressed in the spherical coordinate system) and the horizontal spherical coordinate system is firstly setup. This quadratic polynomial is then transformed to its principal axes. The horizontal principal strains and their orientation in the spherical coordinate system are the corresponding eigenvalues and eigenvectors of this transformation. Moreover, to illustrate the vertical deformations principal strain parameters in the third dimension (vertical component) are interpolated using bi-harmonic spline interpolation technique (Sandwell, 1987). Table 7.6 and Table 7.7 provide the corresponding details.

The computed pattern of vertical deformations is in a good agreement with the one which was proposed in Cohen and Freymueller (1997), see Figure 2.5, in the sense that both match the trend of tectonic features including the Alaska Aleutian trench, the orientation of major

Comp. Point	Contributing points																			df <sub>2d</sub>
	FAIR 1	KOD1 2	KEN1 3	C85G 4	CPRD 5	CROS 6	DAHL 7	GRAV 8	H81D 9	HOMA 10	K76D 11	KIRT 12	M78D 13	NIK2 14	PF12 15	S79R 16	T19D 17	TRLK 18	Z82A 19	
FAIR	-	+	+	+	+	+	+	+	+	+	+	+	+	+	-	+	+	+	+	-
KOD1	+	-	+	+	+	+	+	+	+	+	+	+	+	+	-	+	+	+	+	-
KEN1	+	+	-	×	+	+	×	+	+	×	+	×	+	*	-	×	+	×	+	7
C85G	+	+	+	-	+	+	+	+	+	+	+	+	+	+	-	+	×	×	+	10
CPRD	+	×	×	+	-	+	+	+	+	+	+	+	+	+	-	+	×	+	+	11
CROS	+	+	+	+	×	-	×	+	+	+	*	+	×	+	-	+	+	+	+	10
DAHL	+	+	×	+	+	×	-	+	+	×	×	+	+	+	-	+	×	×	×	7
GRAV	+	+	+	+	+	+	+	-	+	+	+	+	+	+	-	+	+	+	+	14
H81D	+	+	+	+	+	+	+	+	-	+	+	+	+	+	-	+	+	+	+	14
HOMA	+	×	+	+	+	+	+	+	+	-	+	×	+	+	-	+	+	+	+	12
K76D	+	+	+	+	+	*	+	+	+	+	-	+	+	+	-	+	+	+	+	13
KIRT	+	×	+	+	+	+	+	+	+	+	+	-	+	×	-	+	+	+	+	12
M78D	+	×	×	+	+	+	+	+	+	+	+	+	-	×	-	+	+	+	+	11
NIK2	+	+	*	×	+	+	×	+	+	×	+	×	+	-	-	+	+	+	+	9
PF12	-	-	-	-	-	-	-	-	-	-	-	-	-	-	-	-	-	+	-	-
S79R	+	×	+	+	+	+	+	+	+	+	+	+	+	+	-	-	+	+	+	13
T19D	+	+	+	×	+	+	×	+	+	+	+	+	×	+	-	+	-	+	+	11
TRLK	+	+	×	+	+	+	×	+	+	×	+	+	+	+	-	+	×	-	×	9
Z82A	+	+	+	+	+	+	+	+	+	+	+	+	+	+	-	+	+	+	-	14

**Table 7.5:** Configuration of contributing stations for the computation of the deformation tensor at each station in the GPS network of the Kenai Peninsula. The corresponding relative length changes of the stations that are marked with the cross signs in each computation point has been identified as outliers in the two-dimensional approach to the analysis of deformations. Stations that are marked with plus signs contribute in the configuration of contributing points for each computation point. Stars identify the stations whose inclusion in the configuration of contributing points of the corresponding computation points result in the rank deficiency of the system of normal equations.

terrane including the Chugach and Prince William terranes, the strike of the terrane bounding Border Range Fault, the orientation of Cook Inlet and the strike of the Alaska range volcanoes to the west. Cohen and Freymueller (1997) did also claim that not all parts of their pattern was well constrained by the data but, they believed that the overall dome of uplift trending SW to NE and the location of maximum uplift were robust. These features of deformation are also visible in the obtained pattern of vertical deformations in this study.

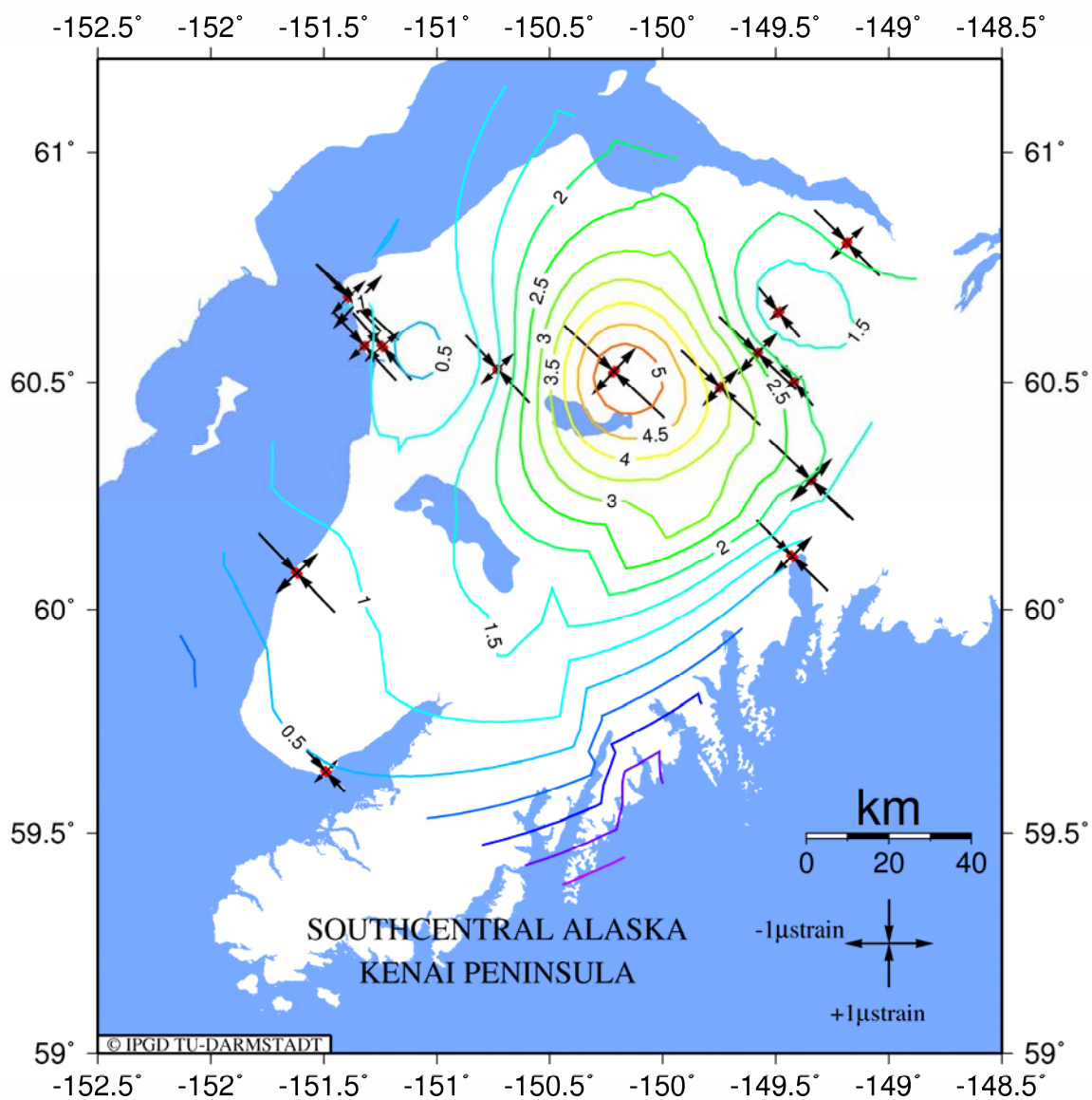


Figure 7.8: 3D-Isoparametric representation of deformations in the Kenai Peninsula.

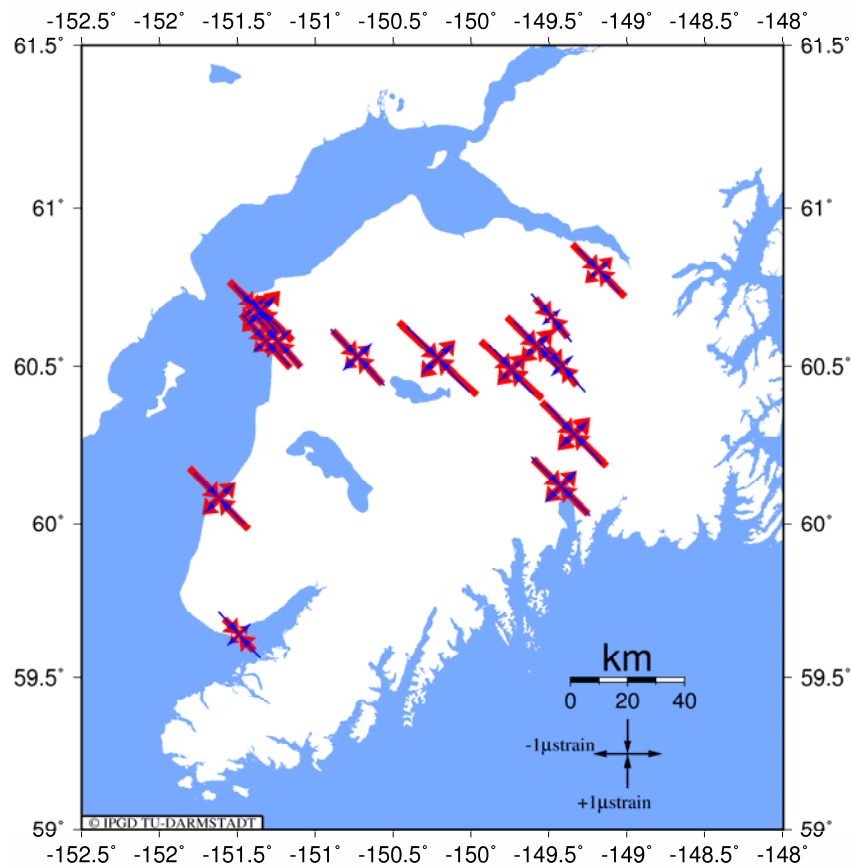
Station Code	Station Name	Horizontal Principal Strains ( $\mu - strain$ )					$\Delta$ ( $\mu - strain$ )	
		$e_I$	$\sigma_{e_I}$	$e_{II}$	$\sigma_{e_{II}}$	Azimuth	$\Delta$	$\sigma_\Delta$
3	KEN1	0.627	0.042	-1.015	0.046	135.05	-0.667	0.073
4	C85G	0.417	0.035	-0.896	0.047	136.69	-0.542	0.250
5	CPRD	0.467	0.045	-0.967	0.047	138.68	-0.618	0.326
6	CROS	0.566	0.055	-1.161	0.047	136.38	-0.806	0.275
7	DAHL	0.351	0.059	-0.910	0.046	139.63	-0.722	0.101
8	GRAV	0.495	0.035	-0.970	0.049	135.56	-0.515	0.321
9	H81D	0.494	0.047	-1.007	0.047	138.42	-0.638	0.319
10	HOMA	0.475	0.034	-0.901	0.049	138.07	-0.492	0.161
11	K76D	0.561	0.038	-1.140	0.058	136.64	-0.605	0.404
12	KIRT	0.476	0.052	-0.971	0.048	139.22	-0.669	0.283
13	M78D	0.660	0.056	-1.300	0.045	138.04	-1.076	0.777
14	NIK2	0.429	0.051	-0.903	0.046	139.12	-0.739	0.110
16	S79R	0.602	0.052	-1.113	0.046	137.82	-0.740	0.862
17	T19D	0.664	0.048	-1.197	0.047	134.19	-0.702	0.312
18	TRLK	0.444	0.053	-1.014	0.045	136.22	-0.713	0.096
19	Z82A	0.585	0.035	-1.040	0.048	135.05	-0.643	0.332

Table 7.6: 3D-Lagrangian principal strains, their 95% confidence intervals and surface compressions.

Station Code	Station Name	Horizontal Principal Strains ( $\mu - strain$ )					$\Delta$ ( $\mu - strain$ )	
		$e_I$	$\sigma_{e_I}$	$e_{II}$	$\sigma_{e_{II}}$	Azimuth	$\Delta$	$\sigma_\Delta$
3	KEN1	0.815	0.107	-1.249	0.182	132.71	-0.551	0.516
4	C85G	0.555	0.163	-1.086	0.094	135.32	-0.957	0.800
5	CPRD	0.603	0.171	-1.223	0.086	133.34	-1.279	2.250
6	CROS	0.621	0.151	-1.196	0.108	134.66	-0.930	0.878
7	DAHL	0.274	0.167	-0.738	0.091	140.23	-0.660	1.000
8	GRAV	0.666	0.154	-1.198	0.105	133.59	-0.968	0.766
9	H81D	0.483	0.145	-1.053	0.116	137.59	-0.792	0.726
10	HOMA	0.364	0.115	-0.626	0.166	136.55	-0.297	0.122
11	K76D	0.682	0.157	-1.311	0.101	134.09	-1.087	1.042
12	KIRT	0.520	0.109	-1.000	0.178	139.05	-0.439	0.697
13	M78D	0.732	0.179	-1.544	0.081	132.77	-1.829	2.144
14	NIK2	0.540	0.120	-1.048	0.157	136.17	-0.622	0.511
16	S79R	0.513	0.147	-1.049	0.113	137.14	-0.765	2.046
17	T19D	0.643	0.108	-1.124	0.181	134.75	-0.513	0.061
18	TRLK	0.249	0.137	-0.693	0.128	142.46	-0.454	0.033
19	Z82A	0.670	0.113	-1.238	0.170	136.27	-0.641	0.174

Table 7.7: 3D-Isoparametric principal strains, their 95% confidence intervals and surface compressions as illustrated in Figure 7.8.

The horizontal patterns of deformations which are obtained from the 3D-Isoparametric and Lagrangian representations of deformation are graphically compared in Figure 7.9. In this figure, arrows in blue and red are used to illustrate the horizontal principal strains of the Lagrangian and Isoparametric approaches respectively. The difference in the magnitude of the



**Figure 7.9: 3D-Isoparametric and 3D-Lagrangian patterns of horizontal deformations in Kenai.**

two sets of results is due to the difference in the resolutions of the corresponding regularized solution. Table 7.8 compares the diagonal elements of the corresponding resolution matrices of the Isoparametric and Lagrangian representations of deformations. The different resolutions of the two sets of results at stations HOMA, T19D, TRLK and Z82A is due to using different regularization parameters for the Isoparametric and Lagrangian representations of deformations. However, sensitivity analysis of the deformation tensor has shown that the sensitivity of the parameters of deformation in the 3D-Isoparametric and Lagrangian repre-

representations of deformation to perturbations of input parameters are different. Therefore, even though in both methods the same number of singular values has been rejected at the other stations, resolution matrices of the corresponding regularized solutions will be different. Table 7.1 shows that for the GPS network of this study and at the level of  $\pm 1$ , the resolution of the horizontal parameters of strain in the 3D-Isoparametric and Lagrangian representations of deformation are the same. Nevertheless, to analyze the accuracy of each solution regularization errors should be assessed. The assessment of regularization error will be discussed in the next section where the two-dimensional results are to be compared with the horizontal components of the 3D-deformation tensors discussed above.

	$e_{xx}$	$e_{yy}$	$e_{xy}$	$e_{zz}$	$e_{xz}$	$e_{yz}$
KEN1	+0.09	-0.05	-0.06	+0.08	+0.11	-0.41
C85G	+0.10	-0.05	-0.06	+0.33	+0.07	-0.67
CPRD	+0.10	-0.06	-0.10	+0.28	+0.15	-0.66
CROS	+0.11	-0.06	-0.10	+0.25	+0.15	-0.62
DAHL	+0.13	-0.05	-0.12	+0.25	+0.18	-0.66
GRAV	+0.11	-0.06	-0.08	+0.33	+0.11	-0.69
H81D	+0.11	-0.06	-0.08	+0.29	+0.13	-0.65
HOMA	-0.02	-0.15	-0.17	-0.12	-0.14	-0.66
K76D	+0.07	-0.05	-0.02	+0.35	+0.00	-0.62
KIRT	+0.10	-0.06	-0.12	+0.21	+0.19	-0.58
M78D	+0.10	-0.06	-0.10	+0.27	+0.15	-0.63
NIK2	+0.10	-0.06	-0.07	+0.24	+0.12	-0.60
S79R	+0.10	-0.06	-0.10	+0.27	+0.16	-0.65
T19D	-0.07	-0.06	-0.15	-0.21	-0.14	-0.65
TRLK	-0.09	-0.06	-0.12	-0.20	-0.12	-0.68
Z82A	-0.03	-0.09	-0.22	-0.15	-0.16	-0.63

**Table 7.8: The comparison of resolution matrices in Isoparametric and Lagrangian representations of deformation.**

The estimated coordinates are also used to see if the infinitesimal theory of strain is sufficient for representing the deformation of this area or the non-linearity of deformations should also be taken into account.

The non-linearity of deformation in any desired direction  $[l, m, n]^T$  is characterized by the quadratic equation: (see Equation 3.18a)

$$\frac{\Delta u^2 + \Delta v^2 + \Delta w^2}{2r^2} = K_{xx} l^2 + K_{yy} m^2 + K_{zz} n^2 + K_{xy} lm + K_{xz} nl + K_{yz} mn \quad (7.2)$$

where,  $r$  is the distance between computation and contributing point and  $\Delta u, \Delta v$  and  $\Delta w$  are the corresponding relative displacements. According to numerical considerations, for the GPS results of the crustal deformation array in the Kenai Peninsula the ratio:

$$q' = \frac{\Delta u^2 + \Delta v^2 + \Delta w^2}{2r^2}$$

is of the order of  $10^{-12}$  and less. However, in estimating the deformations of the order of  $10^{-6}$  (1  $\mu$ -strain) and less numerical precision in arithmetic operations is automatically less than  $10^{-10}$ . Consequently, estimates of this ratio are of the order of computational errors when arithmetic computations are done in double precision. Therefore, their contribution in the relative length changes can be safely ignored. In other words, the infinitesimal theory of strain is self sufficient for analyzing the deformations of this area.

### 3.1. Two-Dimensional versus Three-Dimensional Results

In Figure 7.10, the two-dimensional horizontal pattern of deformations is compared to the horizontal pattern of deformation in the 3D-Isoparametric approach. These parameters have been illustrated by arrows in green. Arrows in red show the corresponding results from the two-dimensional approach. In the eastern Kenai where the topography of the area is rugged, clear differences in terms of the magnitude of the principal strains can be seen between the two sets of results. Figure 7.11 illustrates the pattern of three-dimensional crustal compressions for this area. It is remarkable to note that the place of maximum compression and the place of maximum uplift are conforming together again.

In the two-dimensional approach to the analysis of deformation, the projection of vector lengths onto the surface of the horizontal reference datum takes care of the effect of vertical deformations on the horizontal elements of deformation tensor. Moreover for the few centimeter level vertical deformations in this area, the effect of vertical deformations on the horizontal parameters of strain can be ignored. Therefore, at the first glance these differences

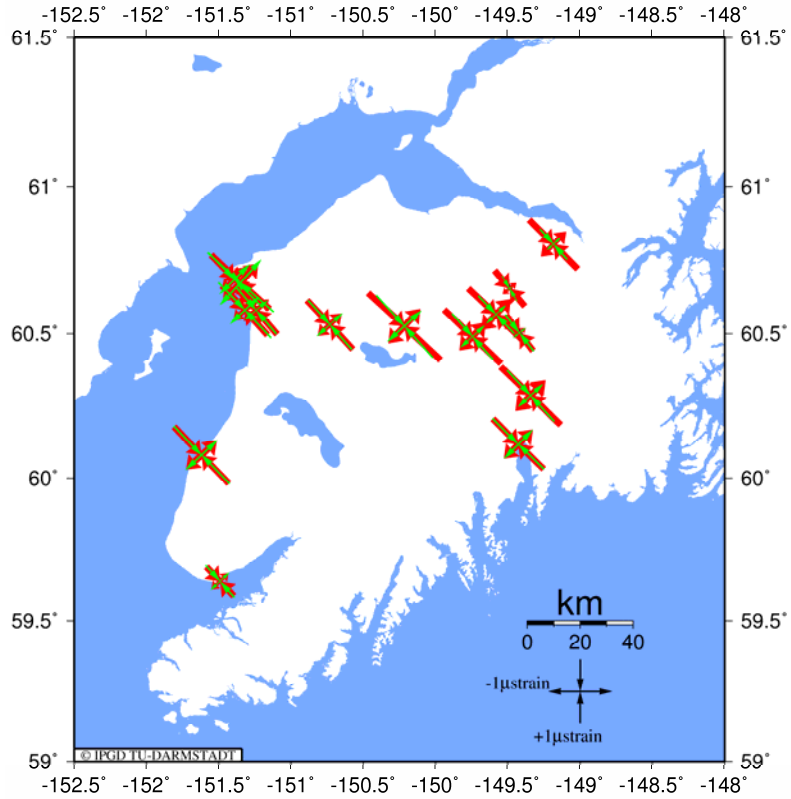


Figure 7.10: Two-dimensional versus three-dimensional pattern of strain in Kenai Peninsula

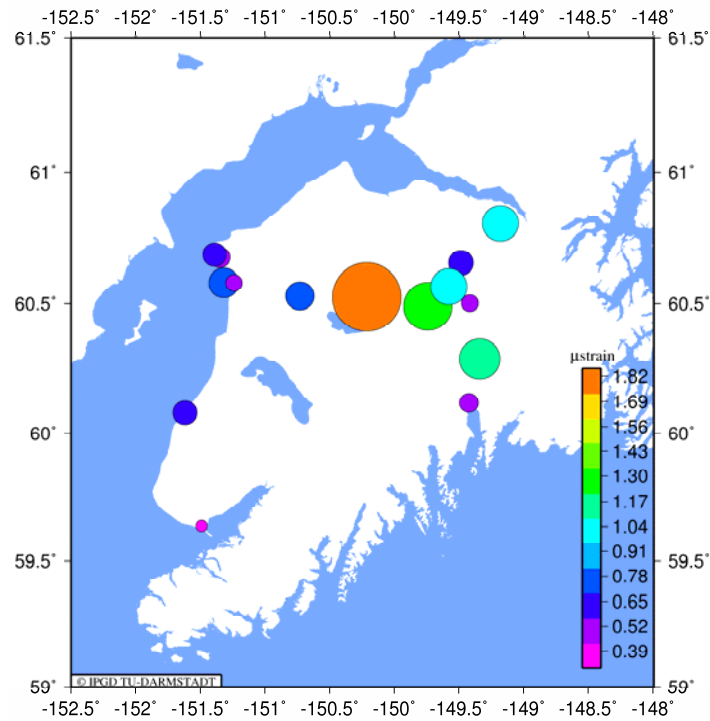


Figure 7.11: Three-dimensional pattern of the Earth's crustal compressions.

are due to the regularization error in the 3D-horizontal parameters of strain. To analyze these differences in further detail, their statistical significance as well as the redundancy of observation in estimating both the two- and three-dimensional deformation tensors should be carefully taken into consideration. To see if the differences mentioned above are stochastically significant their confidence intervals have been computed. Table 7.9 provides the numerical details. In this table parameters  $|\Delta e_I|$  and  $|\Delta e_{II}|$  are the differences of the corresponding horizontal principal strains obtained from the 2D- and 3D- analysis approaches discussed before.  $\sigma_I$  and  $\sigma_{II}$  are the corresponding confidence intervals of these parameters that have been derived by error propagation using the errors of the 2D- and 3D-horizontal principal strains (see Table 7.4, Table 7.6 and Table 7.7). According to Table 7.9, the differences between the 2D-principal strains and the 3D-Lagrangian horizontal principal strains in stations

Station	3D-Isoparametric				3D-Lagrangian			
	$ \Delta e_I $	$\sigma_I$	$ \Delta e_{II} $	$\sigma_{II}$	$ \Delta e_I $	$\sigma_I$	$ \Delta e_{II} $	$\sigma_{II}$
KEN1	0.1580	0.1295	0.1460	0.2030	0.3410	0.0842	0.3800	0.1011
C85G	0.2540	0.2572	0.4490	0.3556	0.1210	0.2021	0.2590	0.3462
CPRD	0.0920	0.2106	0.2590	0.1773	0.0410	0.1310	0.0030	0.1620
CROS	0.1220	0.2482	0.1650	0.2379	0.0680	0.2045	0.1300	0.2171
DAHL	0.1740	0.1931	0.2750	0.1849	0.2550	0.1135	0.4470	0.1674
GRAV	0.2410	0.2945	0.3820	0.3750	0.0760	0.2534	0.1540	0.3633
H81D	0.1530	0.3687	0.1490	0.4319	0.1390	0.3422	0.1950	0.4186
HOMA	0.0360	0.1812	0.0420	0.4220	0.0790	0.1441	0.2330	0.3911
K76D	0.1450	0.2893	0.2180	0.2958	0.0260	0.2460	0.0470	0.2840
KIRT	0.0420	0.2208	0.0350	0.3159	0.0020	0.1989	0.0060	0.2654
M78D	0.0250	0.3940	0.2480	0.4582	0.0450	0.3554	0.0040	0.4532
NIK2	0.1260	0.1791	0.1240	0.2158	0.2370	0.1424	0.2690	0.1550
S79R	0.0370	0.4074	0.0170	0.4737	0.0550	0.3835	0.0810	0.4623
T19D	0.0050	0.2469	0.0060	0.2712	0.0190	0.2271	0.0670	0.2074
TRLK	0.0150	0.1673	0.0250	0.1796	0.1890	0.1097	0.2960	0.1338
Z82A	0.0170	0.3611	0.0170	0.6583	0.1020	0.3448	0.2150	0.6378

**Table 7.9: Regularization errors in the 3D-horizontal principal strains of the Isoparametric and Lagrangian representation of deformation versus the corresponding confidence intervals**

KEN1, DAHL, NIK2 and TRLK are stochastically meaningful. Nevertheless, these differences can not be solely assigned to regularization errors. This is because the redundancies of observations in estimating both the 3D- and 2D-deformation tensors at these stations are

poor. The observational redundancies in both 3D-Isoparametric and Lagrangian representations of deformation can be inferred from the degrees of freedom for the two-dimensional estimates of deformation tensors in Table 7.5. Table 7.9 also shows that in stations KEN1, DAHL and C85G, the differences of the horizontal principal strains of the 3D-Isoparametric and the 2D-Isoparametric approaches are stochastically meaningful. Again since the redundancies of observations in estimating the 2D- and 3D-Isoparametric deformation tensor are small, it is not possible to assign the differences mentioned above only to regularization errors. The results of sensitivity analysis of the deformation tensor have shown that for the GPS network of this study mostly the vertical parameters of deformation are more sensitive to perturbations of inputs. Smaller resolutions of these parameters in the corresponding resolution matrices of both approaches also approve this argument. Therefore, regularization errors of the vertical elements of deformation tensor are larger than the horizontal ones. Nevertheless, the poor redundancy of observations in the GPS network of this study makes the assessment of the regularization error of the vertical parameters of deformation impossible. Otherwise, based on regularization errors of the horizontal parameters of deformation and comparing the resolutions of the vertical and horizontal parameters, estimating an upper bound or a lower bound limit for the regularization error of the vertical parameters of deformation would have been possible. Nevertheless, the fact that the obtained features of vertical deformations in this study conforms to the independent results of other studies shows that regularization errors are not dominating the results of the vertical deformations of this study.

## 7.6. Statistical Inference of Deformations

The estimated velocity field in this study suggests a pattern of spatial variability in the deformation of the Kenai Peninsula. The velocities of the stations in the eastern Kenai are consistent with the relative plate motion of the North American and Pacific Plates derived from a global plate model whereas, the station velocities in the western Kenai are in the opposite direction. The computed relative motion of the North American and Pacific plates is based on the global plate model of DeMets et al., (1990).

To analyze this spatial variation in further detail, the procrustean statistical inference of Chapter 5 has been implemented to the 3D-Isoparametric and Lagrangian estimates of the deformation tensors of this study. Estimated variance-covariance matrices for the 3D-Isoparametric and Lagrangian representations of deformation show a spatial variation in the precision of deformation tensors. The trace of estimated variance-covariance matrices in each approach can be used as a measure for analyzing this spatial variation. In Isoparametric approach this parameter varies from  $\pm 0.03$  to  $\pm 2.25$   $\mu$ -strain whereas in Lagrangian approach the range of variation is between  $\pm 0.07$  and  $\pm 0.86$   $\mu$ -strain. Consequently the minimum detectable variations in the deformation tensors of this area for the Isoparametric and Lagrangian representations are not the same. Also in each method, the minimum detectable change in estimated deformations is variable from one station to another. Therefore, to assess the spatial variations of deformations in Isoparametric and Lagrangian approaches the smallest change that can be commonly detected in all stations of the network and in each method has been used as a threshold for analyzing the spatial variations of deformations in this area. This is nothing else but the minimum internal reliability of the deformation tensor elements in each approach which is computed according to Equation (5.14). For Isoparametric representation of deformation this threshold has been set to  $0.0087$   $\mu$ -strain. In Lagrangian approach this value reduces to  $0.0033$   $\mu$ -strain.

Using a risk level of 5% and a test power of 30%, the spatial variations of the three-dimensional surface deformations have been analyzed. According to this analysis, no significant change between the deformations of two stations GRAV and HOMA can be statistically asserted in Lagrangian representation of deformations in the Kenai Peninsula. The change in deformations of the other stations is stochastically significant for the GPS network in this area. Similar analysis shows that for Isoparametric representation of deformations the deformation changes are stochastically significant between all stations except for the two stations GRAV and K76D. The procrustean statistical inference of estimated deformations shows that the spatial variation of deformations within the Kenai Peninsula, which could also be observed in Figure 7.9 and Figure 7.11, is stochastically meaningful.